

Broadband Channel Characterization in Wooded Environment in the 26 GHz Band

Jean Carneiro da Silva¹, Diego Kasuo Nakata da Silva¹, Leslye Estefania Castro Eras¹, Nadson Welkson Pereira de Souza¹, André Felipe Souza da Cruz¹, Emanuel Costa²
¹Unifesspa, Fl. 31, QD. 7, s/n, 86507-590, Marabá, Brasil. jean.carneiro@unifesspa.edu.br, diegokasuo@unifesspa.edu.br, lecastro@unifesspa.edu.br, nadsonwelkson@unifesspa.edu.br, andacruz@unifesspa.edu.br

²Centro de Estudos em Telecomunicações, Pontifícia Universidade Católica do Rio de Janeiro (CETUC/PUC-Rio), Rua Marquês de São Vicente 225 Gávea, 22451-900 Rio de Janeiro RJ Brasil. epoc@cetuc.puc-rio.br

Abstract— The present work describes the use of a simulation model based on asymptotic methods (ray tracing) on the propagation of ultra-wideband radio signals in a densely-arborized urban channel. The model was previously validated and adjusted using data obtained from measurement campaigns in the millimeter-wave band in locations different from the one to be analyzed here. The simulation uses deterministic methods to predict the received power, cross-polar discrimination, root mean square delay spread, and mean delay in a channel with a high density of scatterers (trees, buildings, and poles). Simulated signals were transmitted in the vertical and horizontal polarizations, considering non-specular reflections caused by rough surfaces and the effect of the transmitter's height variation in outdoor channels.

Index Terms—Deterministic methods, Millimeter-waves, propagation model, Ray tracing.

I. INTRODUCTION

The recent literature on millimeter-wave (mmW) wireless channels is relatively limited. Effectively, the high cost of equipment used in measurement campaigns may limit experimental studies on the use of this frequency band. Thus, several simulation techniques have been proposed [1].

In lower frequency bands, deterministic models based on ray tracing in urban environments provided excellent agreements with results from measurement campaigns [2]. Due to its short wavelength and the possible impact of other important mechanisms, mmW propagation studies should add procedures to the models previously developed for the Very High and Ultra High Frequency bands (VHF and UHF, respectively). Recent studies [3] show that the diffraction mechanism may impose severe losses to the signal, so that coverage in non-line of sight (NLOS) channels may be deficient in the frequency band of interest [4]. On the other hand, small obstacles, and scatters, disregarded in the past, can impact mmW propagation in urban channels. They are present in large quantities, which motivated the inclusion of trees, as well as traffic, energy distribution, and lighting

poles in this simulation.

The 26 GHz band is of interest for the implementation of fifth generation (5G) mobile services in urban environments. Thus, assessing the propagation of mobile communications signals in these environments is important. In these frequencies, waves have limited penetration through constructions and are more subject to small scatters. Thus, their application is usually limited to smaller cells, where the transmitter is located at lower heights and line-of sight (LOS) configurations are preferred [4]. Under these conditions, the vegetation cover present in urban areas can substantially impact signal quality. Therefore, the current work simulates the transmission of signals above, within, and below the canopy layer, in a scenario where the receivers are 1.5 m above the ground.

The next Section describes the ray-tracing model, using Geometric Optics (GO) and the Uniform Theory of Diffraction (UTD). Section III explains several aspects and techniques of the simulation. Section IV shows the results from the simulation along a pre-established route in a square in the city of Belém, based on the metrics: Received power; Cross-polarization discrimination (XPD); Root Mean Square (RMS) delay spread, and the mean delay for ultra-wideband signals (UWB), assuming vertical and horizontal components of the electric field. Finally, Section V analyzes the results from the quantitative and qualitative points of view, outlining future studies.

II. SIMULATION MODEL

The simulation model originated from Silva and Costa [5]-[7]. Initially, the environment is described by a two-dimensional (2D) map, where all buildings bases on a block are grouped and replaced by their polygonal convex hull. Then, each polygon is extrapolated in the vertical direction to form the right prism that represents the corresponding block. The ground is assumed to be plane and horizontal. Each vertical block wall, as well as the ground, has individual constitutive parameters (permittivity, permeability, conductivity, roughness, and dimensions). The atmosphere is modeled as a uniform and isotropic medium in this work, with specific attenuation of the electromagnetic wave described by Recommendation ITU-R P.676-12 [8].

Each tree has a trunk and canopy, represented by concentric right circular cylinders of specified radii and heights. The canopy rests on the trunk. Lighting, energy distribution, and transit poles are also represented by right circular cylinders of specified radii and heights. Satellite maps were used to deploy the trees and poles in the computational representation of the environment as faithfully as possible.

Ray tracing (RT) is based on the image method. Initially, it determines image trees for the (2D) ground projections of the transmitter (Tx), vertical block edges (diffraction points), tree and pole axes, and diffuse reflection points. Each image tree considers up to the eighth order of interaction (specular reflection) with the environment. Initially, 2D rays are traced, using the sets of image trees.

Acceleration techniques which early identify and discard geometrically unrealistic rays were used to optimize the processing time [5]. Subsequently, the model generates 2½D rays between the transmitter and the receiver (Rx), considering each use 2D ray and the difference between the heights of (1) Tx and Rx (to determine the associated aerial ray); (2) Tx and the ground image of Rx (to determine associated ground-reflected rays). However, the model does not consider over-the-rooftop rays.

The propagation mechanisms used in this work, well described in [5]-[7] and summarized in the next Section, are:

- direct ray;
- ground reflection, as well as multiple specular reflections on vertical prism walls;
- single diffraction at vertical prism edges, combined with ground reflection and multiple specular reflections on vertical prism walls;
- single geodetic diffraction by right circular cylinders representing tree trunks and poles, combined with ground reflection and multiple specular reflections on vertical prism walls;
- single scattering by tree canopies, combined with ground reflection and multiple specular reflections on vertical prism walls;
- single diffuse scattering by the rough walls, combined with ground reflection and multiple specular reflections on vertical prism walls;
- attenuation by tree canopies;
- blockages by prisms.

Due to the high losses observed for the diffraction and diffuse scattering mechanisms in the frequency band of interest [3], only rays experiencing at most one of these interactions with the environment were considered.

An IBM PC Intel Core i5 Q6600K with 16 GB DDR4 was used in the simulations, taking an average of 148 minutes for each simulated Rx position.

The radiation diagrams of the Tx and Rx antennas are modeled by the combination of an axially-symmetric Gaussian beam and a constant lateral lobe [9]

$$G(\theta) = G_{max} e^{-4 \ln 2 \left(\frac{\theta}{\theta_{3dB}} \right)^2} + G_o \quad (1)$$

where θ represents the angle between the desired ray direction and the beam axis, G_{max} is the maximum gain, and θ_{3dB} is the half-power beamwidth (HPBW). Assuming that the gain of the lateral lobe G_o is very small, the normalization of (1), integrated over the entire solid angle radiated by the antennas, induces a relationship between G_{max} and θ_{3dB} . The objective is to simulate the effects from highly-directive antennas, with beam axes respectively oriented along the directions of departure (DoD) and arrival (DoA) of the most intense ray identified during the simulation, as expected for 5G technology antennas [10]. Plots associated with equation (1) are available in Recommendation ITU-R P.699-7 [9].

The propagation of electromagnetic fields along the rays is simulated with basis on fundamental theoretical principles: Geometric Optics (GO), and Uniform Theory of Diffraction (UTD). In particular, the mechanisms associated with direct rays, specular reflections, diffraction on vertical edges, reflection and diffraction on cylindrical surfaces, non-specular reflection on rough walls, scattering by tree canopies, and path loss due to tree canopies are individually treated in [11]-[25], respectively, and together in [5]-[7]. Each of the above formulations were validated in several selected environments, described in the appropriate Section.

III. ELECTROMAGNETIC MODELING

A. Polarization of the transmitted signal

The model uses two linearly polarized and orthogonal field components (H: horizontal; and V: vertical) for each ray. In the direct ray mechanism, depolarization does not occur. However, these components may experience depolarization due to the ray interactions with the environment. Thus, each ray can have four combinations of orthogonal components at the observation point, named VV, HH, HV, VH. The first symbol indicates the polarization of the transmitted signal, and the second symbol shows the signal polarization at the observation point (Tx and Rx, respectively).

B. Direct Ray

In this mechanism, there are no interactions of the beam with the environment. The received field \vec{E}_{Rx} is given by

$$\vec{E}_{Rx} = \vec{E}_{Tx} (D \sqrt{G_{Tx} G_{Rx} A_g A_{ef}} e^{-ikr}) \quad (2)$$

where:

- \vec{E}_{Tx} (V/m) is the transmitted field in the desired polarization H or V;
- D (m^{-1}) is the scattering coefficient, equal to $1/r$ for spherical wavefronts, where r (m) is the distance between the Tx and Rx antennas (total path);
- G_{Tx} and G_{Rx} (dimensionless) are the (dimensionless power) gains of the Tx and Rx antennas in the directions of departure and arrival, respectively;

- A_g (dimensionless) is the power loss due to atmospheric gases [8];
- A_{ef} (m²) is the effective reception area, typically $\lambda^2/4\pi$, where λ is the wavelength (m).

C. *Specularly Reflected Rays*

In this mechanism, rays are specularly reflected on the ground or on the vertical prism walls, possibly experiencing multiple interactions of the latter type. For each specular reflection, the incident field is projected onto the plane of incidence (defined by incidence direction and the unit vector orthogonal to the face) and its orthogonal direction. The amplitudes of the projected fields are then multiplied by the (dimensionless) reflection coefficients ($\Gamma_v\rho$) and ($\Gamma_h\rho$), respectively. The results are finally combined into vertical and horizontal components with respect to the reflected ray direction. This process is repeated for all specular reflections of the ray with the environment. This procedure is performed for all field components and specular reflections along a ray. The parameters Γ_v and Γ_h are the Fresnel reflection coefficients [13] for the associated polarization. The factor ρ represents the roughness effects from the reflecting face, which depends on several parameters, which include the standard deviation of the height fluctuations of the irregular surface [14]. The received electric field is calculated by

$$E_{RxPQ} = E_{TxP} \left(D_{PQ} \sqrt{G_{TxP} G_{RxQ} A_g A_{ef}} e^{-ikr} \right) \quad (3)$$

where PQ denotes the combinations HH, HV, VV, VH, the term D_{PQ} (m⁻¹) is equal to the product of all appropriate complex reflection coefficients, divided by r (the sum of the ray segment lengths). The above equation accounts for the effects of multiple specular reflections.

Equations (2) and (3) share the same format and the terms within parentheses indicate the associated ray class contribution to the channel transfer function for each combination of Tx, Rx, polarization (HH, HV, VV, VH), and environment. The contributions from the other interaction mechanisms will be similarly represented.

D. *Rays with a Single Diffraction*

Now, a ray reaches a vertical edge formed by the intersection between two consecutive prism walls.

Initially, the procedure described in Section III.C determines, for each polarization, the incident field component at the diffraction point, considering all possibly existing multiple specular reflections between Tx and this vertex. The ray is then temporarily assumed to consist of two segments. The first is aligned with the real segment ending at the diffraction point, preserving its rectified distance r_1 to Tx and the incident field components. The second is aligned with the real segment beginning at the diffraction point, preserves its rectified distance r_2 to Rx.

Each field component at the diffraction point is then projected onto the incidence plane (defined by direction of the first assumed ray segment and the unit vector aligned with the edge) and the direction

orthogonal to it. The projections are respectively multiplied by the proper diffraction coefficient to determine the projections of the field in the diffraction plane (defined by the direction of the second assumed ray segment and the unit vector aligned with the edge) and the direction orthogonal to it. The diffraction coefficients are obtained from the original UTD formulation by Kouyoumjian and Pathak [21], as modified by Luebbers [15], who introduced reflection coefficients to consider diffraction by edges characterized by faces with finite electromagnetic parameters. In the final step of the diffraction formulation, the results are combined into vertical and horizontal components with respect to the direction of the second assumed ray segment.

If applicable, multiple specular reflections between the diffraction point and Rx are considered, as described in the second paragraph of the present Section.

Each received field component resulting from a single diffraction and multiple specular reflections, using the common notation of (3), is determined by

$$E_{RxPQ} = E_{TxP} \left[D_{PQ} \sqrt{G_{TxP} G_{RxQ}} A_g \frac{r_1}{r_2(r_1+r_2)} e^{-ikr} \right] \quad (4)$$

where the term $D_{PQ}(m^{1/2})$ is the product of the reflection and diffraction coefficients appropriate to the interactions.

The formulation presented in the above paragraphs will also be applied to rays with multiple specular reflections and other single interactions with the environment of a different type (reflection or diffraction by poles or tree trunks; diffuse reflection by a rough wall section; or scattering by a tree canopy). For each ray of any of these classes, the different interaction and multiple specular reflections may occur in any order. The effects from multiple specular reflections (before or after any of the above different interaction) will be treated similarly. Thus, only the formulations for the different interactions will be described in Sections III.F to III.G. The already explained necessary changes to include multiple specular reflection effects will remain implicit.

E. Interactions with Cylinders

Tree trunks and poles are modeled as vertical circular cylinders with proper dielectric constants and conductivities, disregarding diffractions at their tops. The ray-cylinder interaction model adopts the previous temporary assumption of two segments, with respect to the point of interaction with the cylinder. The far end of the first segment and the cylinder define the illuminated and shadow regions.

If the far end of the second segment is in the illuminated region, the cylinder reflects the ray. In this case, considering only the present interaction, the ray contribution to the received field can be expressed by [22]

$$\vec{E}'_{Rx} \approx [R_s E_{\perp}^i(Q_r) \hat{e}_{\perp} + R_h E_{\parallel}^i(Q_r) \hat{e}_{\parallel}^r] \sqrt{\rho_1^r \rho_2^r} \frac{e^{-ikr_2}}{r_2} \quad (5)$$

where:

- $E_{\parallel}^i(Q_r)$ and $E_{\perp}^i(Q_r)$ (V/m) are the complex components of the incident field at the reflection point Q_r in the plane of incidence, defined by the direction of incidence on the cylinder and the normal to the cylinder surface at the interaction point, and the direction orthogonal to the plane of incidence, respectively, considering propagation from Tx to Q_r and including multiple specular reflection effects;
- \hat{e}_{\perp} (dimensionless) is the unit vector orthogonal to the incidence plane;
- \hat{e}_{\parallel}^r (dimensionless) is the unit vector contained in the incidence plane;
- $\rho_{1,2}^r$ (m) are the principal radii of curvature of the reflected wavefront at the far end of the second segment;
- the (dimensionless) reflection coefficients R_s and R_h are determined according to the electromagnetic parameters of the cylinder (for example, $R_{s,h} = \mp 1$ for perfect electrical conductors, respectively; for tree trunks, $R_{s,h}$ are provided by the heuristic Luebbers formulation for the appropriate polarization [15]).

If the far end of the second segment is in the shadow region, the mechanism that transports energy is diffraction around the cylinder surface. The segments are adjusted so that the incident ray becomes tangentially touches the cylinder surface, propagates along the surface and tangentially emerges from it towards the far end of the second segment. Considering only the diffraction effect, the electric field at the Rx can be represented by [22]

$$\vec{E}'_{Rx} \approx [T_s E_{b1}(Q_1) \hat{b}_2 + T_h E_{n1}(Q_1) \hat{n}_2] \sqrt{\rho_2^d} \frac{e^{-iks^d}}{s^d} \quad (6)$$

Let $\hat{t}_{1,2}$ and $\hat{n}_{1,2}$ be the (dimensionless) tangent and normal unit vectors out of the cylinder at the incidence and emerging points $Q_{1,2}$, respectively. In equation (6), the (dimensionless) unit vectors are defined by $\hat{b}_{1,2} = \hat{t}_{1,2} \times \hat{n}_{1,2}$ at these points, respectively. Additionally, $E_{b1}(Q_1)$ and $E_{n1}(Q_1)$ (V/m) are the respective components of the electric field incident on Q_1 in the directions of \hat{b}_1 and \hat{n}_1 , which consider propagation from Tx to Q_1 (including multiple specular reflection effects); $\rho_2^d = s^i + t$, where s^i (m) is the rectified distance from Q_1 to the far end of the first segment and t (m) is the length of the ray arc (Q_1, Q_2) along the cylinder surface; and s^d (m) is the rectified distance from Q_2 to the far end of the second segment. Finally, T_s and T_h ($m^{1/2}$) are the diffraction coefficients for the associated polarization [16], [22].

If applicable, multiple specular reflection effects from Q_r or Q_2 to Rx should be included. Finally, $(G_{TxP}G_{RxQ}A_g)^{1/2}$ multiplies each component of the received field.

F. Diffuse Reflections from Rough Walls

The diffuse reflection model is suffered by lightning and is represented by the equation [17], [23]

$$P_{Rx} = \frac{1}{4\pi} P_{Tx} G_{Tx}(\theta_T) RCS \left(\frac{\lambda}{4\pi R_T R_R} \right)^2 G_{Rx}(\theta_R) \quad (7)$$

where P_{Tx} (W) is the transmitted power; $G_{Tx}(\theta_T)$ is the (dimensionless) gain of the transmitter antenna; the angle between the Tx beam axis and the direction of departure (from Tx to the scattering point) is θ_T (rad); R_T (m) is the distance from Tx to the scattering point; $G_{Rx}(\theta_R)$, θ_R and R_R are analogous parameters associated with Rx and the scattering; and λ (m) is the wavelength of the transmitted signal. Finally, RCS (m^2) is the radar cross section of the wall section, represented by

$$RCS = A_{eff} \cos \theta_i S^2 f_{ge}^2(\theta_s, \varphi_s) \quad (8)$$

where A_{eff} (m^2) is the effective illuminated area. In combination with the radiation pattern of the Tx antenna, it is estimated by

$$G_{Tx}(\theta_T) A_{eff} = \sum_{n=1}^N G_{Tx}(\theta_{Tn}) \delta A_n \quad (9)$$

where N is the total number of sections assumed on the wall, δA_n (m^2) is the corresponding section area, and θ_{Tn} (rad) is the angle between the segment joining Tx to the center of the section and the beam axis. The current implementation assumes $N = 3$ and the average value of the Tx and Rx antenna heights determines the section centers. It is important to note that, depending on the Tx antenna radiation pattern, A_{eff} may be less than the total area of corresponding section.

In (8), θ_i (rad) is the angle between the incident ray direction and the normal to the wall section; $S^2 = (1 - \beta)$ is the (dimensionless) fraction of the incident power that is scattered. This factor can be approximated by $\beta \approx (|\Gamma|\rho)^2$, if the power transmitted through the wall is neglected [10], [17]. The (dimensionless) term $f_{ge}^2(\theta_s, \varphi_s)$ represents the angular distribution of the power scattered by each rough wall section, which can be modeled by [16]

$$f_{ge}^2(\theta_s, \varphi_s) = f_n \left\{ F \cos \theta_s + (1 - F) \left[\left(\frac{1 + \cos \psi_R}{2} \right)^{\alpha_R} \right] \right\} \quad (10)$$

The angular distribution model combines the Lambertian and Directional formulations, according to the multiplication factors F ($0 \leq F \leq 1$) and $(1 - F)$. The normalization term f_n ensures that the integral of $f_{ge}^2(\theta_s, \varphi_s)$ over the applicable hemisphere is equal to one. The angle ψ_R (dependent on θ_s and φ_s) is measured from the hypothetical specular reflection direction and the directivity of the second component increases with α_R . Fig. 1 shows normalized diagrams associated with (10) in the

plane of incidence (defined by the direction of incidence and the normal to the rough wall), setting the specular reflection angle to 45° and assuming the following parameter combinations: (1) $F = 1.0$ (Lambertian scattering, purple); (2) ($F = 0.8, \alpha_R = 6$) (blue); (3) $F = 0.6$ and $\alpha_R = 6$, used in the simulation to be described (red); (4) $F = 0.2$ and $\alpha_R = 6$ (green); and (5) $F = 0.2$ and $\alpha_R = 20$ (black), which emphasize the function of the directional component.

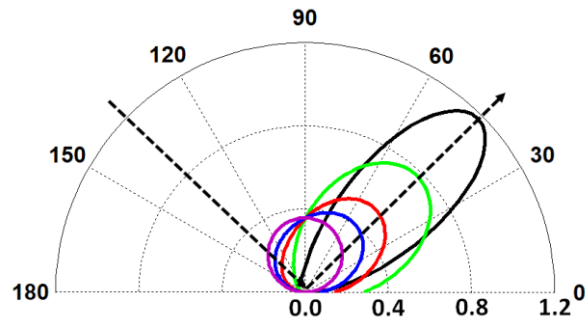


Fig. 1. Diffuse scattering diagram in the incidence plane with parameters: (1) $F = 1.0$ (Lambertian scattering, purple); (2) ($F = 0.8, \alpha_R = 6$) (blue); (3) $F = 0.6$ and $\alpha_R = 6$, used in the simulation to be described (red); (4) $F = 0.2$ and $\alpha_R = 6$ (green); and (5) $F = 0.2$ and $\alpha_R = 20$ (black).

The diffuse reflection mechanism results from many micro-interactions caused by the wall roughness and the resulting field at the receiver is considered incoherent and non-polarized [17], [18]. Therefore, the resulting field is represented by the combination of two orthogonal linearly polarized components with the same absolute value. Simultaneously, their phases are randomly and independently sorted, using a uniform distribution in the interval $[0, 2\pi)$. In more detail, the square root of the power ratio in (7), considering (8), produces:

$$\chi = \sqrt{P_{Rx}/P_{Tx}} = |\vec{E}_{Rx}|/|\vec{E}_{Tx}| = \frac{\lambda}{4\pi R_T R_R} f_{ge}(\theta_s, \varphi_s) \times \sqrt{\frac{G_{Tx}(\theta_T) G_{Rx}(\theta_R)}{4\pi} A_{eff} (1 - \beta) \cos\theta_i} \quad (11)$$

where $|\vec{E}_{Rx}|$ and $|\vec{E}_{Tx}|$ are the absolute values of the received and transmitted field, respectively. Thus, for each component of the transmitted field and each wall section, the received field resulting from diffuse reflection is represented by

$$\vec{E}_{Rx} = \frac{1}{\sqrt{2}} \chi |\vec{E}_{Tx}| \sqrt{A_g} (e^{-i\varphi_1} \hat{\theta}_s + e^{-i\varphi_2} \hat{\varphi}_s) \quad (12)$$

where $\hat{\theta}_s$ and $\hat{\varphi}_s$ are unit vectors orthogonal to each other and to the segment that connects the center of the wall section center to Rx, while φ_1 and φ_2 are independent random variables uniformly

distributed in the interval $[0, 2\pi)$.

G. Scattering by Tree Canopies

Energy scattering by tree canopies is an electromagnetic problem of great complexity. The implementation used by the present version of the model has a relatively low computational cost and was adjusted to anechoic chamber measurement results using a few tree species. The work of Caldeirinha and Al-Nuaimi [24] is the basis for the implementation. The (dimensionless) normalized scattering pattern that characterizes the power received at an observation point is approximated by

$$D_n(\theta) = \frac{4\alpha\beta_s^{-2} e^{-\left(\frac{\theta}{\beta_s}\right)^2} + (1 - \alpha)}{4\alpha\beta_s^{-2} + (1 - \alpha)} \tag{13}$$

where the scattering angle θ is defined from the incidence direction and $D_n(0) = 1$. The scattering pattern combines a Gaussian beam with an isotropic component $(1 - \alpha)$, where α (rad) is the ratio between the forward and the total scattered powers. Two measurement campaigns at 20 GHz and 62.4 GHz validated the model, which also estimated good adjustment values for its parameters ($\beta_s = \pi/12$ rad and $\alpha = 0.5$ rad).

Very similar results were observed, in that study, for both orthogonal polarizations. A study of independent experimental results [25] indicated that the scattered signal phase and polarization are randomly distributed. Thus, the scattered field results combine two orthogonal components $E_{SH,V}$ with common intensity and random phases. Each component is represented by

$$E_{SH,V} = \frac{1}{\sqrt{2}} |E_{inc}| \sqrt{(1 - \xi) D_n(\theta)} e^{-i\varphi_{H,V}} \tag{14}$$

where $|E_{inc}|$ (V/m) is the absolute value of the incident field; ξ ($0 \leq \xi \leq 1$) is the fraction of the incident power absorbed by the tree top; and $\varphi_{H,V}$ are independent random phases, uniformly distributed in the interval $[0, 2\pi)$.

H. Power Loss Associated with Propagation Through Vegetation

All fields associated with rays that intercept tree canopies experience additional attenuation. This phenomenon is distinct from the scattering due to tree canopies described in the previous section. Each component of the electric field associated with a ray that intercepts tree canopies is multiplied by:

$$10^{-\frac{\gamma_t d_t}{20}} e^{-j\varphi} \tag{15}$$

where γ_t is the specific attenuation for canopy propagation (dB/m) [19], [20]; d_t (m) is the total length of the ray inside tree canopies; and φ is a random phase uniformly distributed in the interval $[0, 2\pi)$. Recommendation ITU-R P.833-9 [19], based on the *Radiative Energy Transfer* (RET) method, indicates that γ_t has a linear dependence on the operation frequency. It should be noted that the RET

calculation model for isolated trees in Recommendation ITU-R P.833-9 [19] is based on the frequency (GHz), typical leaf size and the leaf area index (LAI) of the tree species. Mango tree leaf lengths and widths range from 150 mm to 400 mm and 60 mm to 160 mm, with mean values 243.44 mm and 55.74 mm, respectively. Their average length/width ratio equals 4.37 [26]. Mango tree cultivars exhibit LAI values in the range (1.18, 4.48), with mean value 2.94 [27]. These parameters substantially differ from most listed in Recommendation ITU-R P.833-9 [19]. Additionally, to circumvent the complexities involved in the association of RET calculations with ray tracing, the present model approach considers the total route through canopies, where the specific attenuation was adjusted to trees located in the cities of Rio de Janeiro and Belém [5],[28].

In summary, many 2½D individual rays (in some cases, more than 100,000) are traced between the Tx and Rx antennas. Each ray belongs to a class (with multiple specular reflections; with single diffraction or scattering, combined or not with multiple specular reflections in any order; etc.). The Tx antenna emits H and V components, independently tracked along each ray, as a result, considering the interactions with the environment and the proper algorithms described in Sections III.B to III.G, the co- and cross-polarized field components (HH, HV, VH, and VV) due to each ray are calculated at the Rx antenna. The total field component received for any polarization combination results from the sum of the complex contributions from all the individual rays, weighted by the TX and Rx antenna patterns, atmospheric losses, and attenuation due to propagation through tree canopies (according to the formulation in Section III.H). Appendix I shows a simplified block diagram of the electromagnetic calculation for each ray class in this model.

IV. SIMULATION

In the simulation model, a channel is characterized by the Tx and Rx antenna positions, orientations of their main beams, emitted and received field polarizations and the environment. The estimated channel transfer function $H(f)$ is specified over a UWB frequency spectrum, discretized into a large number of uniformly spaced frequencies. Thus, $H(f)$ is calculated, for each discretized frequency, by the sum described in the last paragraph of the previous Section. Applying the fast inverse Fourier transform (IFFT) to the transfer function $H(f)$, the impulse response is obtained, which can be used to determine the power delay profile (PDP) of the channel. The numerical integration of the PDP over the delay domain yields the received power. From the PDP, the mean delay and RMS delay spread can be estimated. The XPD is calculated by the ratio between the received powers associated with the co- and cross-polarized components of the electric field, as described in [3], [5], [12].

The simulation implements the Beam Combination technique [29] by aligning of the main beam axes of the Tx and Rx antennas with the directions of departure (DoD) and arrival (DoA) of the ray with the most intense electric field.

The *Praça da República* in Belém, Pará, Brazil, shown in the overview of Fig. 2, was chosen as the

simulation environment. The square is heavily arborized and surrounded by multi-story buildings. Its southern and northern sides have the tallest buildings, with dozens of floors. The Tx was located at a fixed position, at heights of 3 m, 12 m, and 30 m above the ground. This height variation evaluated the effects of propagation for Tx below, between, and above the canopy layer. The dimensions of the mango (*Mangifera Indica*) trees located in the square were obtained from previous campaigns carried out by Silva et al. [26], who studied propagation in urban vegetation areas, identifying an average total height of 20.0 m. The canopies start at an average height of 3.8 m. The canopies and tree trunks have average diameters of 12.0 m and 0.5 m, respectively. The Rx was displaced along a pre-established route at uniform intervals of 20.0 m, always at the height of 1.5 m from the plane and horizontal ground.



Fig. 2. Three-dimensional photo of *Praça da República* in Belém, Pará, Brazil, with a predominance of mango (*Mangifera Indica*) trees on its outer edges, with sparse vegetation inside. [Adapted from Google Maps].

Fig. 3 describes the environment and the Tx (yellow circle) and Rx (red circles) positions along the selected route. The transmitter Tx is located at the center of the square's north face, without building or tree obstructions within a radius of 25.0 m. The square is surrounded by leafy trees along its outer edges, with sparse vegetation inside. Table I shows the transceiver locations, the distance between Tx and Rx, and the number of rays detected for each simulated Rx position.

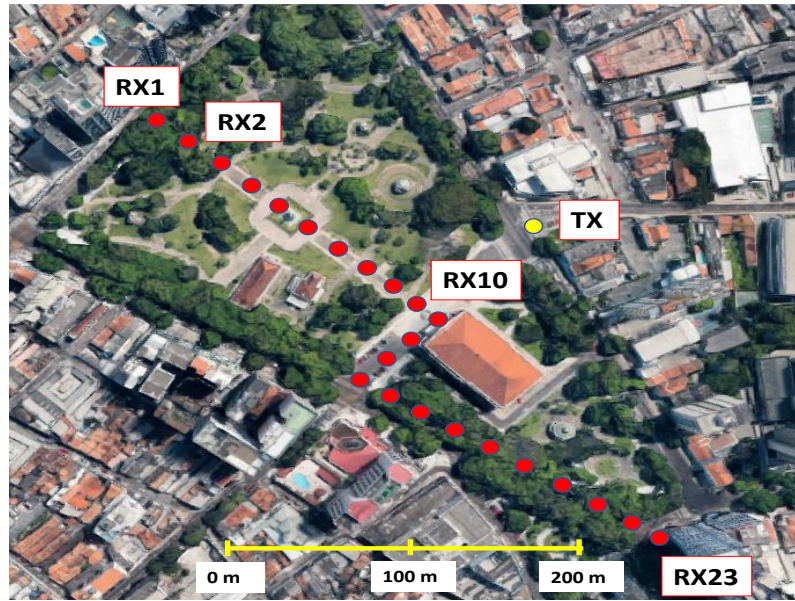


Fig. 3. Tx (yellow circle) and Rx positions along the route (red circles). [Adapted from Google Maps]

TABLE I. TX AND RX POSITIONS, DISTANCES AND NUMBERS OF ASSOCIATED RAYS

Id	Position	DistanceTx- Rx (m)	Numbers of Rays
TX	1 27 07 S 48 29 36 W	0.0	
Rx1	1 27 05 S 48 29 43 W	230.5	73256
Rx2	1 27 05 S 48 29 42 W	209.6	69444
Rx3	1 27 06 S 48 29 42 W	191.1	71852
Rx4	1 27 06 S 48 29 41 W	175.4	77984
Rx5	1 27 07 S 48 29 41 W	157.5	59738
Rx6	1 27 07 S 48 29 40 W	137.9	66082
Rx7	1 27 07 S 48 29 40 W	125.7	74016
Rx8	1 27 08 S 48 29 39 W	113.6	67160
Rx9	1 27 08 S 48 29 39 W	101.7	62878
Rx10	1 27 09 S 48 29 38 W	93.1	55462
Rx11	1 27 09 S 48 29 38 W	88.5	52770
Rx12	1 27 10 S 48 29 38 W	107.2	58914
Rx13	1 27 10 S 48 29 39 W	126.2	50228
Rx14	1 27 11 S 48 29 39 W	145.6	61988
Rx15	1 27 12 S 48 29 39 W	142.8	48656
Rx16	1 27 12 S 48 29 38 W	146.7	35780
Rx17	1 27 12 S 48 29 37 W	147.6	33654
Rx18	1 27 13 S 48 29 37 W	152.4	41662
Rx19	1 27 13 S 48 29 36 W	155.9	48004

DOI: <http://dx.doi.org/10.1590/2179-10742021v20i4254762>

Rx20	1 27 13 S 48 29 35 W	161.5	57840
Rx21	1 27 14 S 48 29 35 W	171.8	69210
Rx22	1 27 14 S 48 29 34 W	186.4	60580
Rx23	1 27 15 S 48 29 33 W	202.2	53308

The first three Rx positions are close to the west edge, inside an area with several trees. From Rx4 to Rx9, the route crosses the center of the square, with less vegetation. Rx10 to Rx14 display LOS propagation conditions. On the other hand, the direct links from Tx to each of receiver positions Rx15 to Rx19 are blocked by *Teatro da Paz*, which is the largest building inside the square. The last five Rx positions are located on the southern edge of the square, surrounded by trees.

Fig. 4 describes the computational representation of the environment: green and black circles represent tree and pole projections, respectively, and black polygons represent the prism ground projections. The previous color code identifies the Tx (yellow circle) and Rx positions along the route.

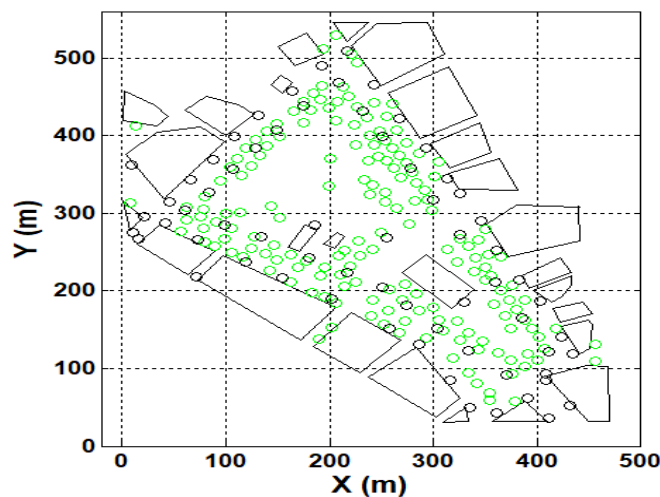


Fig. 4. Computational representation of the environment: green and black circles represent tree and pole projections, respectively; black polygons represent the prism ground projections.

The simulation was performed at the center frequency of 26 GHz, assuming the transmission of a UWB signal with uniform power spectral density along a 500 MHz bandwidth. The Tx and Rx antennas have a maximum gain of 24 dBi and 10° HPBW. The power transmitted for all polarizations was 1 W. The ground and building walls have a dielectric constant $\epsilon_r = 3$, conductivity $\sigma = 15$ mS/m, and roughness $\sigma_h = 0.75$ mm. The specific attenuation due to atmospheric gases is $\gamma = 0.1$ dB/km, and the specific attenuation due to tree tops linearly varies in the range [6.83 dB/m, 6.98 dB/m] over the frequency band, modeled according to [5] and [28]. The adopted diffuse scattering model combined the Lambertian and Directional components according to (10), with $F = 0.6$ and directivity factor $\alpha_R = 6$ [5]. The perfect electric conducting poles have a height of 10.0 m and a diameter of 0.3 m [28]. For each simulated Rx channel, the axes of the Tx and Rx antenna beams respectively align with the DoD

and DoA directions of the ray with the greatest electric field intensity.

V. RESULTS

A. Ray Tracing

Table I established that Rx15 to Rx19, with direct rays blocked by *Teatro da Paz*, were reached by a significantly smaller number of rays than all the other receivers, including those located at the end of the route (Rx21 to Rx23). Receivers Rx1 to Rx3 and Rx20 to Rx22, located inside areas with several trees, and Rx4 to Rx9, located in the center of the square, were reached by the largest number of rays. It is noted that these numbers are greater than the ones associated with most of the receivers that operate under LOS conditions (Rx10 to Rx13). These observations are mainly credited to tree scattering effects, less important in the region of the last receiver group, less vegetated than the others.

Fig. 5 plots the rays associated with Tx-Rx1 (surrounded by trees) and Tx-Rx17 (NLOS), identified by the large red and green circles. Black polygons represent the prism projections. Red asterisks and triangles represent scatterers and diffraction points, respectively. Rays specularly reflected, diffracted and scattered by trees, poles, or rough walls, are represented by blue, magenta, and green lines, respectively. It is noted that reflections by the building walls (in special, those facing the square) confine the energy inside the square. The relative importance of scattering is evident in Panel (b). However, the contribution of specular reflection and the scattering from trees, poles, and rough surfaces surrounding Rx1 should also be identified in Panel (a).

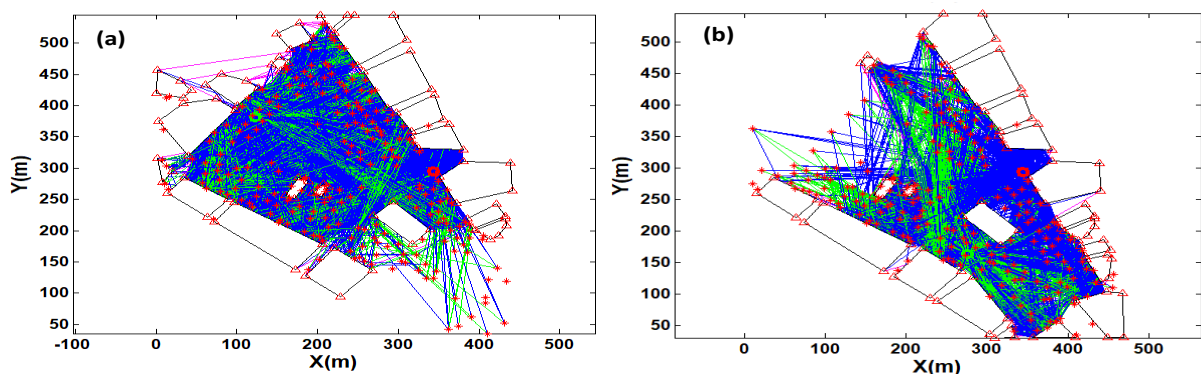


Fig. 5. Panel (a) presents ray tracing results for Rx1; Panel (b) shows ray tracing results for Rx17, using the same convention, described in the text.

B. Received Power

For each Tx height, Rx location, and polarization combination, the received power was calculated as described in the last paragraph of Section III and the first paragraph of Section IV. Fig. 6 shows the variation of the power received by each Rx, considering different Tx heights above the ground (below, within, or above the canopy layer), for the co-polarization combinations VV or HH. The simulation for $h_{Tx} = 3$ m indicates decreases in the powers received by Rx2 and Rx4 that are

approximately equal to 30 dB and 20 dB, relative to those of the neighbor receivers, regardless of the above polarization combinations. These excess attenuations are due to blockages of the corresponding direct rays by tree trunks. It is observed that the received power remains relatively constant for Rx9 and the LOS channels Rx10 to Rx14, since the direct rays experience small attenuations or remain totally unblocked. The *Teatro da Paz* building blocks the direct beams Tx-Rx16 to Tx-Rx19, causing a sharp decrease in the corresponding received powers. For the $h_{Tx} = 12$ m simulation, most rays associated with Rx1 to Rx6 and Rx16 to Rx23 intercept the tree canopies (regardless of their positions relative to Tx and the receivers), being severely attenuated for both attenuation combinations. On the other hand, the received power levels for Rx9 and the LOS channels Rx10 to Rx14 remain close to the previous ones, since the corresponding direct rays were not substantially affected by the increase of the Tx height. The simulation results for $h_{Tx} = 30$ m are similar to the ones corresponding to $h_{Tx} = 12$ m. However, there is a sharp decrease noted in the powers received by Rx16 to Rx22, because the rays traced from Tx at a greater height now interact with the canopies.

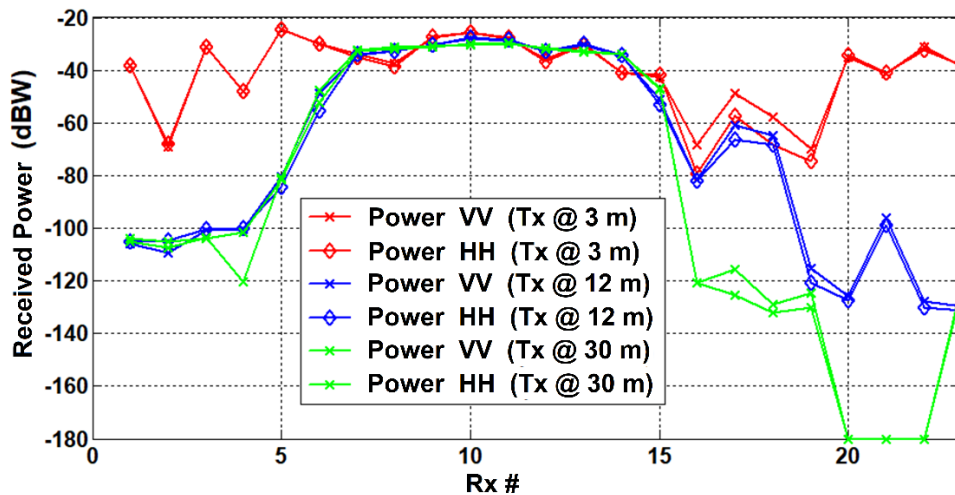


Fig.6. Received powers estimated for all 23 receivers, the VV and HH polarizations and Tx heights above ground.

C. Mean Delay

Fig. 7 illustrates the simulated values for the mean delay, using only the vertical component. The mean delays for the initial receivers show high values that decrease until Rx11, which has the shortest distance to Tx. Then, it increases with the distance to Tx. The simulation for $h_{Tx} = 3$ m indicates an increase in the mean delay for Rx2, relative to those for the neighbor receivers, due to the blockage of the corresponding direct ray by a tree trunk. A substantial increase in the mean delays for Rx15 to Rx19, due to the NLOS condition forced by the *Teatro da Paz* building. This condition remains until Rx20, which resumes the previous smooth increase related with the Tx-Rx distance. For the simulations associated with $h_{Tx} = 12$ m and $h_{Tx} = 30$ m, this metric displays a similar general behavior. However, the effects from propagation through and scattering due to tree canopies are observed in the time delays for Rx1 to Rx6 and Rx16 to Rx23.

D. RMS Delay Spread

Fig. 8 shows the variation of the RMS delay spread, strongly affected by the type of ray reaching the Rx. The direct and specular reflection rays generally display higher powers and smaller delays than those associated with scattering or diffraction. Their presence favors small values of the RMS delay spread. The simulation for $h_{Tx} = 3$ m shows a substantial variation of RMS delay spread at Rx positions close to vegetation and with attenuated (or blocked) direct rays. These conditions generally increase the relative powers of scattered or diffracted rays, with disperse delays. This condition increases the RMS delay spread. Indeed, the channels operating under strict or approximate LOS conditions consistently displayed low values for the present metric, for all Tx heights. The other receivers showed substantial variations for the RMS delay spread, due to ray interactions with the tree tops. The present observations are in good agreement with those available in the literature [7].

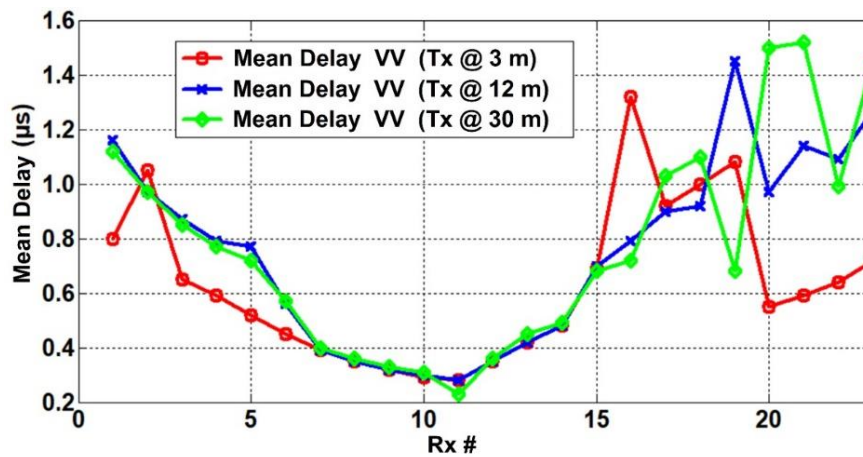


Fig.7. Mean delay estimated for all 23 receivers and Tx heights, with minor variations observed for strict or approximate LOS conditions.

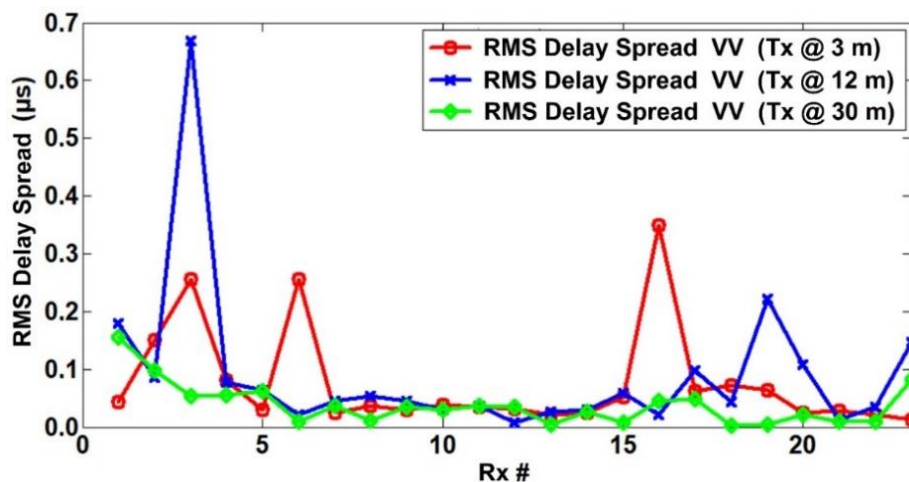


Fig.8. RMS delay spread estimated for the 23 receivers and Tx heights, with minor variations observed for strict or

approximate LOS conditions.

E. XPD

Fig. 9 illustrates the behavior of $XPD_{VH} = 20 \log |E_{HH}/E_{VH}|$ and $XPD_{HV} = 20 \log |E_{VV}/E_{HV}|$, which show opposite effects to those observed in the RMS delay spread. Their values increase with the predominance of the direct and reflected rays, reaching their highest values. It is possible to observe the substantial variation of this metric as a function of the predominant mechanisms of the rays reaching each Rx. In general, the results for the receivers affected by scattering (Rx1-Rx6 and Rx20-Rx23, particularly for $h_{Tx} = 12$ m and $h_{Tx} = 30$ m) or operating under NLOS conditions (Rx16-Rx19, for all Tx heights) display the smallest XPD values.

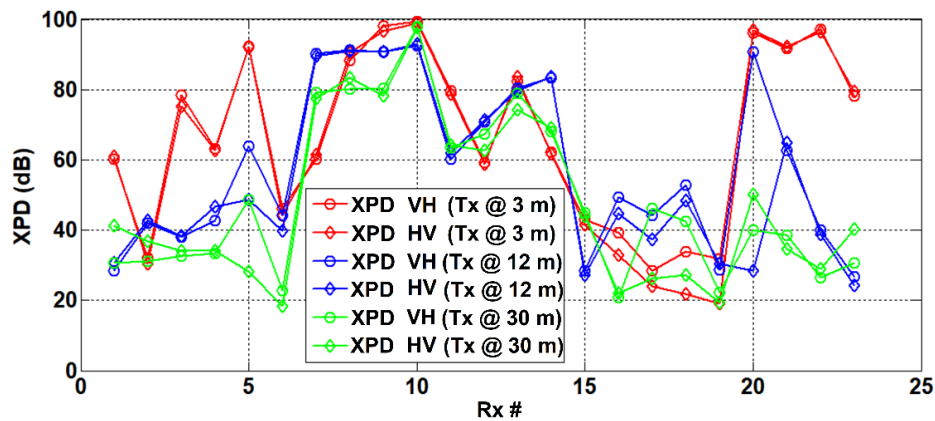


Fig.9. XPD between co-polarized and crossed signals. It is possible to notice substantial variation, caused mainly by trees close to the receivers.

VI. CONCLUSION AND FUTURE WORK

In this work, it was evident that the analyzed metrics showed better results in channels displaying strict or approximate LOS conditions. Trees and other scatterers can substantially impact the propagation of millimeterwaves, and consequently degrade the performance of UWB systems operating in this frequency band.

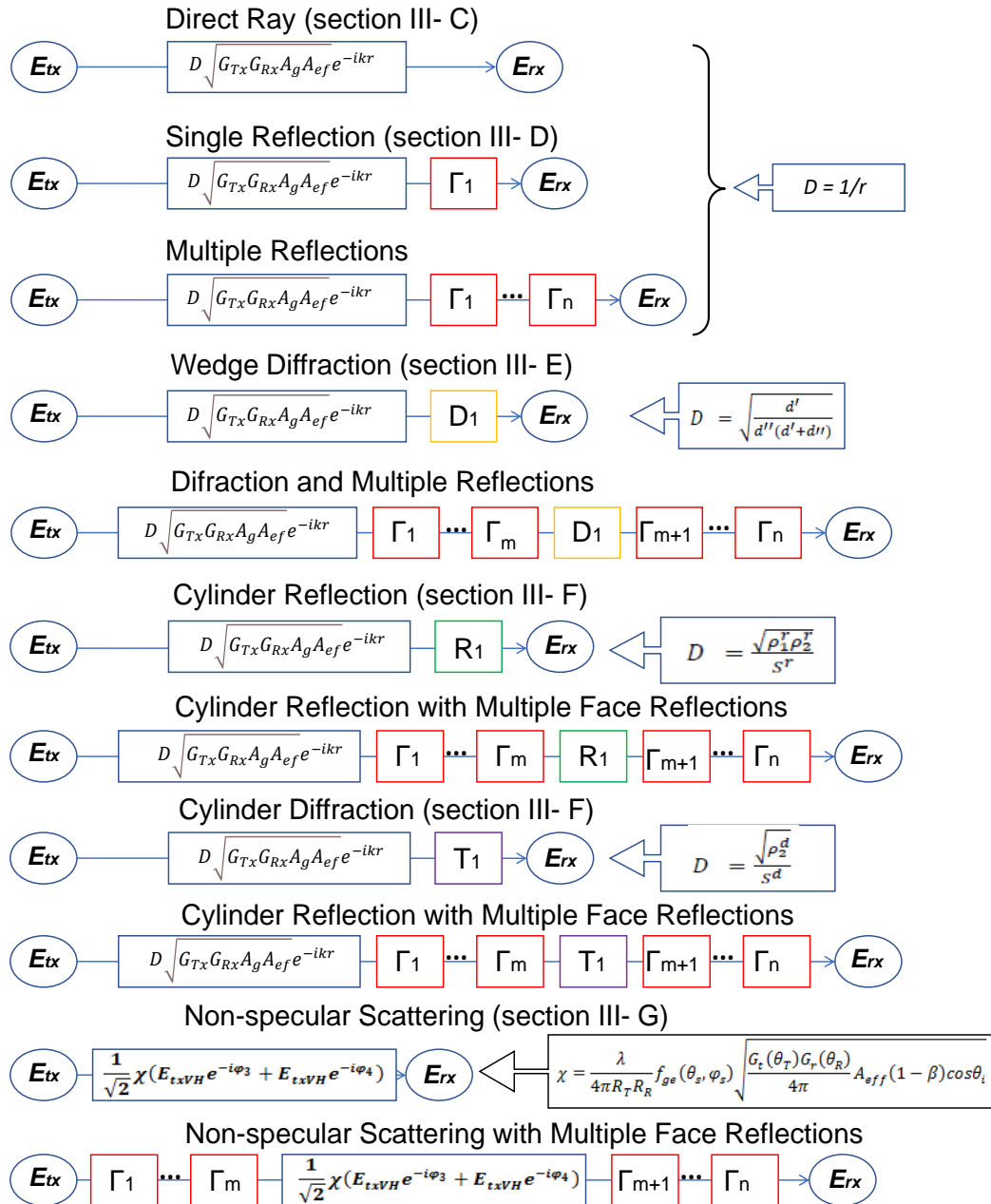
As expected, excess attenuations in the received power were observed in response to blockages of the corresponding direct rays by tree trunks and the *Teatro da Paz* building, as well as by propagation through tree canopies. The mean delay depends on the distance from Tx to Rx, being also affected by NLOS conditions forced by tree trunks and the *Teatro da Paz* building, as well as by propagation through and scattering due to tree canopies. The dominance of direct and specular reflection rays generally favors small values of the RMS delay spread. On the other hand, the simulation results show substantial variations of the RMS delay spread at Rx positions close to vegetation and with attenuated (or blocked) direct rays. These conditions generally increase the relative contributions of scattered or diffracted rays, increasing the RMS delay spread. The results also show XPD behaviors in opposition to those observed in the RMS delay spread. The Tx height effects on these parameters were discussed.

Possible extensions of the current simulation model should consider the effects from other scatterers, such as vehicles (parked or in motion), traffic-control plates and persons. Rain attenuation and scattering are also extremely important in the millimeter-wave band. It should be remembered that the current model version is based on the 2½D ray-tracing technique, which assumes building blocks with infinite heights. In principle, a full 3D model could be developed to consider building blocks with finite heights and over-the-rooftop rays. However, the additional complexity should be weighted by the multiple-diffraction effects that would be present in these rays, tending to severely attenuate the associated fields.

The study will also proceed with the simulation of the channel behavior in new bands and other environments, combined with the possible comparison with data obtained in measurement campaigns performed in urban regions with dense tree coverages.

APPENDIX I

The diagram summarizes the application of the formalism described in section III and shows the field calculation at the receiver for each ray type. Note that the red, yellow, green and purple boxes represent the application of the respective coefficients described for each case. Additionally, an attenuation power loss is applied if any tree canopy interception occurs.



ACKNOWLEDGMENT

This study was financed in part by *Coordenação de Aperfeiçoamento de Pessoal de Nível Superior - Brasil (CAPES)* - Finance Code 001. E. Costa is supported by CNPq award PQ 305984/2019-5.

REFERENCES

- [1] M. Shafi, A. F. Molish, P. J. Smith, T. Haustein, P. Zhu, P. De Silva, F. Tufvesson, A. Benjebbour, and G. Wunder, "5G: A tutorial overview of standards, trials, challenges, deployment, and practice", *IEEE J. Select. Areas Comm.*, vol. 35, no. 6, pp. 1201-1221, 2017.
- [2] M. C. Lawton and J. P. McGeehan, "The application of a deterministic ray launching algorithm for the prediction of radio channel characteristics in a small-cell environment", *IEEE Trans. Antennas Propag.*, vol. 43, no. 4, pp. 955-968, 1994.
- [3] T. S. Rappaport, R. W. Heath Jr., R. C. Daniels, and J. N. Murdock, *Millimeter Wave Wireless Communications*. New York, NY, USA: Prentice Hall, 2015, pp. 83-135.
- [4] S. Salous, V. Degli-Esposti, F. Fuschini, D. Dupleich, R. Müller, R. S. Thomä, K. Haneda, J. M. M. G. Pardo, J. P. Garcia, D. P. Gaillot, M. Nekovee, and S. Hur, "Millimeter-wave propagation: characterization and modelling toward

DOI: <http://dx.doi.org/10.1590/2179-10742021v20i4254762>

- fifth-generation systems”, *IEEE Antennas Propag. Mag.*, vol. 58, no. 6, pp.115-127, 2016.
- [5] J. C. Silva, “Modelo determinístico de propagação de ondas milimétricas em ambientes com alta densidade de espalhadores”, Tese de Doutorado, CETUC/DEE, Pontifícia Universidade Católica do Rio de Janeiro, Rio de Janeiro, RJ, Brazil, 2019.
- [6] J. C. Silva and E. Costa, “Modelo de propagação de ondas milimétricas em ambientes urbanos com alta densidade de espalhadores”. In: XXXV Simpósio Brasileiro de Telecomunicações e Processamento de Sinais (SBRT2017), vol. 1, pp. 383-387, São Pedro, SP, Brasil, 2017.
- [7] J. C. Silva and E. Costa, “UWB millimeter wave propagation model for realistic outdoor environments: dense scatter by trees and non-specular scattering effects”. In: 2018 IEEE AP-S and URSI USNC Joint Meeting (AP-S/URSI 2018), 2018, Boston, MA, USA, 2018.
- [8] International Telecommunication Union, “Attenuation by atmospheric gases”, Recommendation ITU-R P.676-12, Geneva, Switzerland, 2019.
- [9] International Telecommunication Union, “Reference radiation patterns for fixed wireless system antennas for use in coordination studies and interference assessment in the frequency range from 100 MHz to about 70 GHz”, Recommendation ITU-R F.699-8, Geneva, Switzerland, 2018.
- [10] T. S. Rappaport, S. Sun, R. Mayzus, H. Zhao, Y. Azar, K. Wang, G. N. Wong, J. K. Schulz, M. Samimi, and F. Gutierrez, “Millimeter wave mobile communications for 5G cellular: it will work!”, *IEEE Access*, vol. 1, pp. 335-249, 2013.
- [11] H. W. Son, and N. H. Myung, “A deterministic ray tube method for microcellular wave propagation model”, *IEEE Trans. Antennas Propag.*, vol. 47, no. 8, pp. 1344-1350, 1999.
- [12] H. L. Bertoni, *Radio Propagation for Modern Wireless Systems*. New York, NY, USA: Prentice Hall PTR, 2000.
- [13] S. Hussein, and C. Brennan, “Efficient preprocessed ray tracing for 5G mobile transmitter scenario in urban microcellular environments”, *IEEE Trans. Antennas Propag.*, vol. 67, no. 5, pp. 3323-3333, 2019.
- [14] H. L. Bertoni, *Radio Propagation for Modern Wireless Systems*. New York, NY: Prentice Hall PTR, 2000.
- [15] R. J. Luebbers, “A heuristic UTD slope diffraction coefficient for rough lossy wedges,” *IEEE Trans. Antennas Propag.*, vol. 37, no. 2, pp. 206-211, 1989.
- [16] S. W. Lee, “Differential geometry for GTD applications,” Electromagnetics Lab. Report, University of Illinois, Urbana, IL, Rep. 77-21, 1977.
- [17] V. Degli-Esposti, F. Fuschini, E. M. Vitucci, and G. Falciasecca, “Measurement and modeling of scattering from buildings,” *IEEE Trans. Antennas Propag.*, vol. 55, no.11, pp. 143-153, 2007.
- [18] V. Degli-Esposti, “A Diffuse scattering model for urban propagation prediction”, *IEEE Trans. Antennas Propag.*, vol. 49, no. 7, pp. 1111-1113, 2001.
- [19] International Telecommunication Union, “Attenuation in vegetation”, Recommendation ITU-R P.833-9, Geneva, Switzerland, 2016.
- [20] M. A. Weissberger, “An initial critical summary of models for predicting the attenuation of radio waves by trees”, EMC Analysis Center Report TR-81-101, Annapolis, MD, USA, 1982.
- [21] R. G. Kouyoumjian and P. H. Pathak, “A uniform geometrical theory of diffraction for an edge in a perfect conducting surface”, *Proc. IEEE*, vol. 62, no. 11, pp. 1448-1461, 1974.
- [22] P. H. Pathak, W. D. Burnside, and R. J. Marhefka, “A uniform GTD analysis of the diffraction of electromagnetic waves by a smooth convex surface”, *IEEE Trans. Antennas Propag.*, vol. 28, no. 5, pp. 631-642, 1980.
- [23] V. Degli-Esposti, “A diffuse scattering model for urban propagation prediction”, *IEEE Trans. Antennas Propag.*, vol. 49, no. 7, pp. 1111-1113, 2001.
- [24] R. F. S. Caldeirinha and M. O. Al-Nuaimi, “Propagation modelling of bistatic scattering of isolated trees for micro and millimeter wave urban microcells”, In: *13th IEEE Int. Symp. Pers. Indoor Mob. Radio Comm.*, Lisbon, Portugal, 2002, pp. 135-139.
- [25] S. A. Torrico, H. L. Bertoni, and R. H. Lang, “Modeling tree effects on path loss in a residential environment”, *IEEE Trans. Antennas Propag.*, vol. 46, no. 6, pp. 872-880, 1998.
- [26] J. C. Vieccelli, D. L. de Siqueira, W. M. S. Bispo, and L. M. C. Lemos, “Characterization of leaves and fruits of mango (*mangifera indica L.*) cv. Imbu”, *Rev. Bras. Frutic., Jaboticabal - SP*, vol. 38, no. 3:e-193, pp. 1-7, 2016.

DOI:<http://dx.doi.org/10.1590/2179-10742021v20i4254762>

- [27] S. Rajan, R. Kumar, and S. S. Negi, "Variation in canopy characteristics of mango (*Mangifera indica* L.) cultivars from diverse eco-geographical regions", *J. Appl. Hort.*, vol. 3, no. 2, pp. 95-97, 2001.
- [28] J. C. Silva, G. L. Siqueira, and P. V. G. Castellanos, "Propagation model for path loss through vegetated environments at 700-800 MHz band", *Journal Microw. Opt. Electrom. Applic.*, vol. 17, no. 1, pp. 179-187, 2018.
- [29] H. Yan, G. R. MacCartney Jr., S. Sun, and T. S. Rappaport, "5G millimeter-wave channel model alliance measurement parameter, scenario parameter, and measured path loss data list", NYU Wireless Rep. TR2016-002, New York University, New York, NY, USA, 2016.